GOES 8 aerosol optical thickness assimilation in a mesoscale model: Online integration of aerosol radiative effects

Jun Wang, U. S. Nair, and Sundar A. Christopher

Department of Atmospheric Sciences, University of Alabama in Huntsville, Huntsville, Alabama, USA

Received 26 March 2004; revised 4 August 2004; accepted 12 August 2004; published XX Month 2004.

[1] To investigate the importance of aerosol radiative effects in the troposphere, numerical simulation of a dust event during the Puerto Rico Dust Experiment is presented by using the Colorado State University Regional Atmospheric Modeling System (RAMS). Through assimilation of geostationary satellite-derived aerosol optical thickness (AOT) into the RAMS, spatial and temporal aerosol distribution is optimally characterized, facilitating direct comparison with surface observations of downwelling radiative energy fluxes and 2 m air temperature that is not possible with a free-running mesoscale model. Two simulations with and without consideration of aerosol radiative effects are performed. Comparisons against observations show that direct online integration of aerosol radiative effects produces realistic downwelling shortwave and longwave fluxes at the surface but minimal improvement on 2 m air temperature at the observation location. Numerical simulations show that for the dust loading considered in this study (AOT = 0.45 at 0.67 μm), if the dust radiative effects are not properly represented, the uncertainty in the simulated AOT is about ±5 to ±10%, the surface radiative energy is overestimated by 30–40 W m^{-2} during the day and underestimated by 10 W m^{-2} during the night, and the bias in air temperatures near the surface could be up to ±0.5°C, though these biases also depend on local time, AOT values, and surface properties. The results from this study demonstrate that the assimilation of satellite aerosol retrievals not only improves the aerosol forecasts but also has the potential to reduce the uncertainties in modeling the surface energy budget and other associated atmospheric processes. INDEX TERMS: 3337 Meteorology and Atmospheric Dynamics: Numerical modeling and data assimilation; 0305 Atmospheric Composition and Structure: Aerosols and particles (0345, 4801); 3359 Meteorology and Atmospheric Dynamics: Radiative processes; KEYWORDS: satellite assimilation in mesoscale model, GOES 8 aerosol optical thickness, radiative effects

Citation: Wang, J., U. S. Nair, and S. A. Christopher (2004), GOES 8 aerosol optical thickness assimilation in a mesoscale model: Online integration of aerosol radiative effects, *J. Geophys. Res.*, *109*, XXXXXX, doi:10.1029/2004JD004827.

1. Introduction

[2] Dust, a common aerosol over the desert, can be transported to downwind areas thousands of kilometers away from source regions [*Reid et al.*, 2003], degrading visibility and air quality, perturbing the radiative transfer in the atmosphere [*Hansen and Lacis*, 1990], providing a vector for disease-causing organisms [*Shinn et al.*, 2000], and exacerbating symptoms in people with asthma [*Prospero*, 1999]. On the other hand, the atmospheric deposition of dust aerosols containing iron and other trace elements is an important nutrient source for the oceanic biota [*Duce*, 1991]. Both satellite remote sensing [*Christopher and Zhang*, 2002; *Wang and Christopher*, 2003] and numerical models [*Tegen and Fung*, 1994; *Weaver et al.*, 2002] have been used to study dust radiative effects and to monitor pollution.

[3] Satellite remote sensing data sets are widely used to map the geographical distribution of aerosols at high spatial and temporal resolutions and to explore the effects of atmospheric aerosols on the Earth's radiation budget [*Kaufman et al.*, 2002]. However, numerical models are the preferred tool for studying the role of tropospheric aerosols in modulating several important atmospheric processes such as surface radiation energetics and atmospheric heating rates [*Carlson and Benjamin*, 1980]. Currently, satellite-derived aerosol information is not commonly used in numerical models, especially regional models. Using a case study of a dust event observed during the Puerto Rico Dust Experiment (PRIDE) [*Reid et al.*, 2003], we explore the utility of assimilating satellite-derived aerosol information into numerical models to examine aerosol radiative effects.

[4] The majority of Sun-synchronous polar-orbiting satellites provides global images approximately once a day and can only provide snapshots of large-scale aerosol spatial distribution during the time of satellite overpass. On the other hand, each geostationary satellite can view about

0148-0227/04/2004JD004827$09.00

one third of the globe at temporal resolutions up to 15 min or higher and is therefore suitable for the tracking, monitoring, and validation of regional-scale aerosol events [*Wang et al.*, 2003]. Recent advances in satellite retrievals can qualitatively capture aerosol optical thickness (AOT) distribution with high spatial [*Kaufman et al.*, 2002] and temporal resolutions [*Christopher et al.*, 2002; *Wang et al.*, 2003]. These satellite retrievals play an important role in the estimation of aerosol radiative forcing [*Christopher and Zhang*, 2002] and validation of numerical models [*Chin et al.*, 2002]. However, current aerosol retrievals such as AOT are mostly column quantities, thereby making it difficult for examining the vertical distribution of aerosols and their associated changes of radiative transfer in the atmosphere [*Kaufman et al.*, 2002].

[5] Numerical models, both global and regional, are used to forecast the three-dimensional (3-D) aerosol distributions. Compared to global simulations, regional mesoscale models have finer spatial grids and therefore can be used in the study of transport dynamics [*Westphal et al.*, 1987, 1988; *Colarco et al.*, 2003], aerosol radiative forcing [*Collins et al.*, 2001], and modeling of air pollution [*Binkowski and Roselle*, 2003]. Most regional models are off-line models [*Byun and Ching*, 1999], where the simulations are externally driven by meteorological fields derived from other numerical models (such as Pennsylvania State University/National Center for Atmospheric Research Mesoscale Model (NCAR MM5) or global climate models). Few regional-scale models explicitly include the radiative interactions in aerosol transport simulations, yet the radiative effect of dust aerosols can exert important effects on the forecast of meteorological fields such as surface temperature and boundary layer process, thereby motivating accurate characterization of aerosols in model simulations [*Carlson and Benjamin*, 1980; *Yu et al.*, 2002].

[6] Limited availability of ground-based aerosol observations, especially over the oceans, constrains the accuracy of initial aerosol fields in both global and regional chemical transport models (CTMs) [*Westphal and Toon*, 1991; *Chin et al.*, 2002]. In general, in most numerical simulations, dust emission occurs when the wind speed over an erodible surface exceeds some threshold value. The choice of wind speed threshold and parameterization of the emission flux is highly variable for different regions and is treated differently in numerical modeling studies even for the same area [*Takemura et al.*, 2000; *Ginoux et al.*, 2001; *Colarco et al.*, 2003]. Further challenges also exist in regional aerosol models that attempt to study the aerosol in one region but must span a large domain in order to capture the dust transport approaching from dust source region into the area of interest. This requires the use of nested grid configurations that add significant computational overhead to numerical simulations.

[7] Assimilation of satellite aerosol retrievals circumvents many of the problems associated with initializing aerosol field in regional simulations. The assimilation of aerosol information derived from satellite measurements is a valuable tool to characterize the aerosol initial condition in the model, constrain the model simulation, and improve the model forecast [e.g., *Collins et al.*, 2001; *Yu et al.*, 2003]. Previous studies [*Collins et al.*, 2001; *Yu et al.*, 2003] have assimilated the aerosol retrievals from polar-orbiting satellite into off-line models and showed that the assimilation of satellite-retrieved AOT significantly improved the performance of aerosol simulations. Although these studies utilized satellite-derived AOT to represent aerosol spatial distribution, they did not consider aerosol radiative effects nor the possible atmosphere response to the aerosol radiative effects such as change of atmospheric radiative heating rate and surface radiative energy budget during the simulation, since aerosol transport was modeled in an "off-line" mode. Furthermore, polar-orbiting satellites used in these studies have a repeat cycle of 1∼2 days which is insufficient to capture the temporal evolution of the aerosol field. Field experiments with intensive observations therefore provide a good opportunity to investigate aerosol radiative effects in numerical models. During PRIDE [*Reid et al.*, 2003], half-hourly dust AOT distribution over the ocean in the vicinity of Puerto Rico was retrieved from the GOES 8 imager [*Wang et al.*, 2003]. Through assimilating GOES 8 AOT into the Colorado State University Regional Atmospheric Modeling System (CSU RAMS) [*Pielke et al.*, 1992], and by using observation data sets during PRIDE, this study examines the radiative effects of dust aerosols.

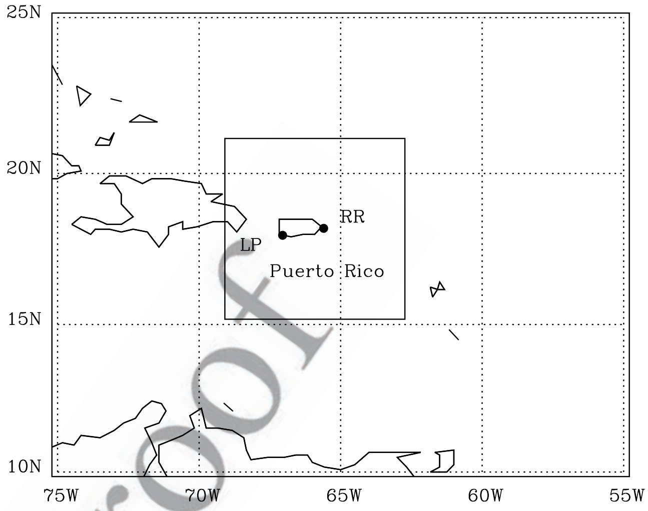

Figure 1. Model domain where the inset rectangle shows the domain of the fine grid. Also shown are the locations where the ground-based measurements were made at Roosevelt Road ((RR) 18.20°N, 65.60°W) and La Paguera ((LP) 17.97°N, 67.05°W).

2. Data and the Area of Study

[8] The area of study (Figure 1) is centered on Puerto Rico, which was also the base for PRIDE [*Reid et al.*, 2003]. Of the five major dust events that were recorded during PRIDE, we study the most severe event that occurred during 20∼23 July 2000 (see Figure 2, A1–A5, and detailed description in section 5.1). Profiles of aerosol concentration from aircraft measurements, longwave and shortwave downward radiative flux (W m^{-2}) data from Surface Measurements for Atmospheric Radiative Transfer (SMART) [*Ji and Tsay*, 2000], Sun photometer inferred AOT, and 2 m air temperature measurements made during PRIDE are used. The location of two Sun photometers are

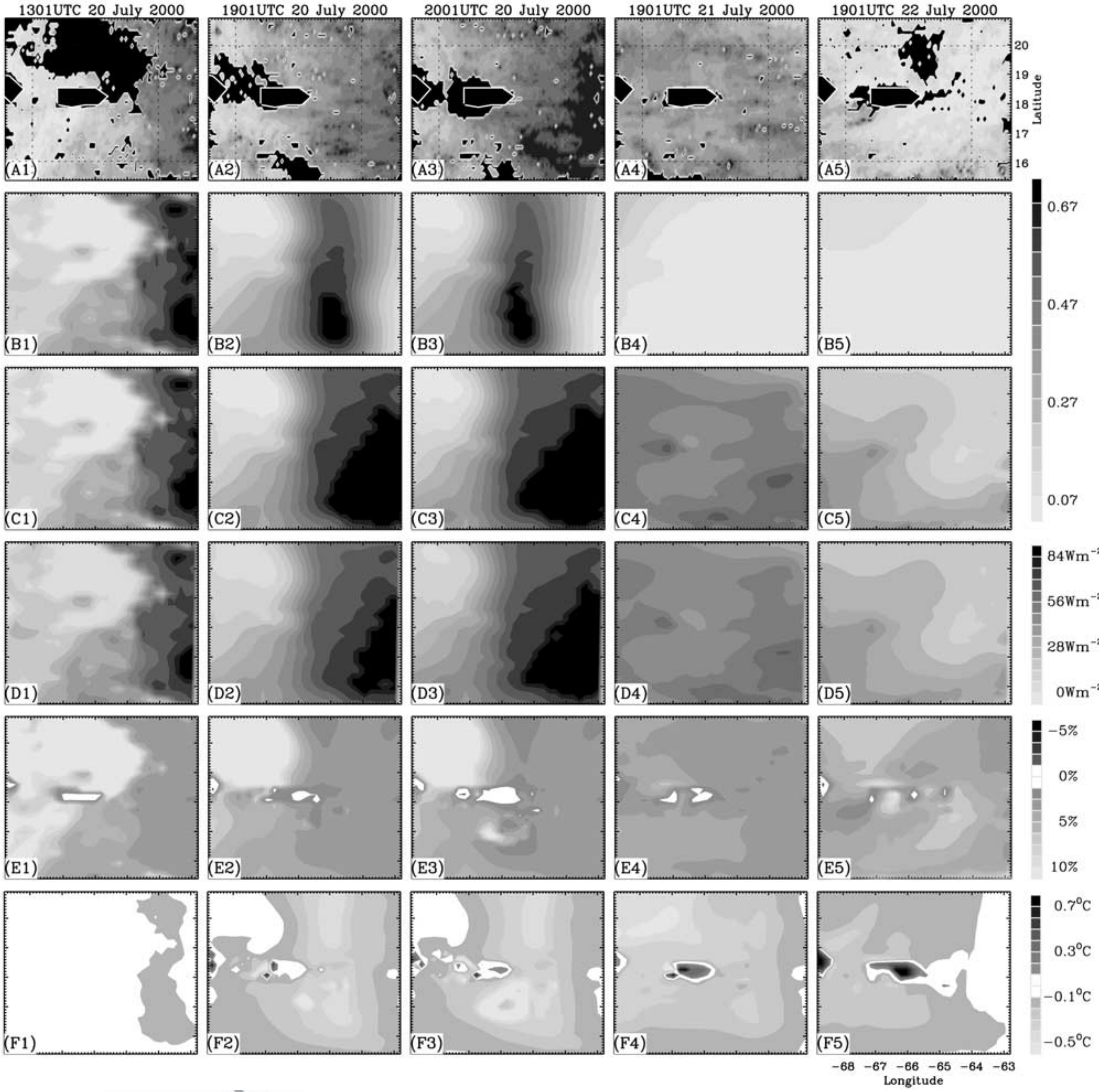

Figure 2. Dust AOT retrieved from GOES 8 (A1–A5) and simulated AOT from the RAMS with (B1–B5) and without (C1–C5) assimilation of GOES 8 AOTs using nudging scheme. The percentage difference in AOT between aero-rad and noaero-rad cases is shown in D1–D5. The total downward radiative flux difference (longwave plus shortwave, W m^{-2}) at the surface and temperature difference (°C) in the model first layer above the surface are shown in E1–E5 and F1–F5, respectively. The black regions in A1–A5 are cloudy regions, and the white-outlined black areas are Puerto Rico land regions. See color version of this figure at back of this issue.

shown in Figure 1 including Roosevelt Road ((RR) 18.20°N, 65.60°W) and La Paguera ((LP) 17.97°N, 67.05°W). However, for this study, only AOT at LP is used, since data at RR during 20∼23 July 2000 were not available. Further details regarding the data sets are given by *Reid et al* [2003].

[9] During PRIDE, dust AOTs retrieved from the GOES 8 imager [*Wang et al.*, 2003] were used for studying the diurnal change of dust forcing at the top of atmosphere (TOA) and at the surface [*Christopher et al.*, 2003]. Using light scattering, absorption, and size distribution measurements, the refractive index and single scattering albedo of dust aerosols were estimated to be 1.53−0.0015i and 0.98 at 0.55 μm, respectively [*Wang et al.*, 2003]. These aerosol optical properties are then used in a discrete ordinate radiative transfer model to create look-up tables for the GOES 8 AOT retrievals. The satellite retrievals compared well with both in situ and ground-based Sun photometer measurements [*Wang et al.*, 2003].

[10] The National Center for Environmental Prediction (NCEP) reanalysis atmospheric data [*Kalnay et al.*, 1996] at 0000, 0600, 1200 and 1800 UTC are used as a first guess for creating analysis of the meteorological fields used for specifying the initial conditions of the numerical model and for the evolution of the lateral boundary conditions for simulations starting at 1200 UTC on 20 July 2000 and ending at 1200 UTC on 23 July 2000. In addition, radiosonde and surface meteorological data obtained from data sets maintained at NCAR are also utilized in analysis of these meteorological fields. Standard databases available with the RAMS (version 4.3) are used to initialize topography and land use type at each grid cell while sea surface temperature is initialized using the National Oceanic and Atmospheric Administration (NOAA) satellite-derived values (J. Vazquez et al., NOAA/NASA advanced very high resolution radiometer (AVHRR) Oceans Pathfinder Sea Surface Temperature Data Set User's Reference Manual Version 4.0, JPL Publication D-14070, available at http://www.nodc.noaa.gov/woce_V2/disk13/avhrr/docs/usr_gde4_0_toc.htm).

3. Methodology

[11] The CSU RAMS (version 4.3) [*Pielke et al.*, 1992] is modified to assimilate the GOES 8 AOT. Currently, the RAMS does not include dust aerosols in the radiative transfer calculations. Therefore the RAMS was modified to include a sophisticated δ four stream radiative transfer model (δ4S RTM) [*Liou et al.*, 1988; *Fu and Liou*, 1993] that includes dust aerosol radiative properties measured during PRIDE [*Christopher et al.*, 2003]. The aerosol transport model is built upon a tracer advection module in the RAMS combined with additional specification of source and sink mechanisms.

3.1. Description of the CSU RAMS and New Modifications

[12] The RAMS is a nonhydrostatic atmospheric model [*Pielke et al.*, 1992] that has been successfully used to simulate a wide range of atmospheric phenomenon including sea breezes, severe storms, flash flooding, downslope winds, air pollution, and atmospheric convection ranging from boundary layer cumulus to mesoscale convective systems [*Cotton et al.*, 2002]. The RAMS utilizes finite difference approximations to solve conservation equations of mass, momentum, heat, and different phases of water on a polar stereographic grid in the horizontal and a terrain following sigma coordinate system in the vertical. At large horizontal spatial scales, the RAMS uses convective parameterization schemes to account for precipitation mechanisms, while at smaller spatial scales it provides the capability to resolve cloud and precipitation processes through explicit bulk water parameterization. Surface layer parameterization along with a multilayer soil model and the sophisticated Land Ecosystem Atmosphere Feedback model (LEAF-2) [*Walko et al.*, 2000] account for exchanges of energy and momentum fluxes between the surface and the atmosphere. The RAMS also provides a wide range of techniques for representing subgrid-scale turbulence and top and lateral boundary conditions. It includes a data analysis/assimilation module which blends upper air, surface observations and gridded data from other models such as NCEP reanalysis data to create products that are used for initializing the model and nudging the top and lateral boundaries of the model. The RAMS provides three options of varying sophistication for longwave and shortwave radiation calculations. However, none of three existing radiation schemes in the RAMS accounts for the radiative interactions of aerosols. Hence the δ4S RTM is implemented in the RAMS to compute the aerosol radiative effects online.

3.1.1. The δ4S RTM

[13] The δ4S RTM is a plane-parallel broadband radiative transfer model, originally designed to calculate the radiative flux at TOA and surface in clear and cloudy conditions [*Fu and Liou*, 1993] and later modified for calculation of radiative effect of aerosols, such as smoke [*Christopher et al.*, 2000] and dust [*Christopher et al.*, 2003]. Gas absorption, water vapor absorption, and Rayleigh scattering are included in the model calculations. The model divides the shortwave (SW) spectrum (0.2∼4 μm) into six bands and further divides the first band (0.2–0.7 μm) into 10 subbands. The longwave (LW) spectrum is divided into 12 bands from 4 to 35.7 μm. To treat the radiative transfer accurately, the δ4S RTM uses a δ function to better represent the phase function in the forward scattering direction [*Liou et al.*, 1988]. For the principal atmospheric gases the difference between the δ4S RTM and line-by-line irradiance calculations is within 0.05% [*Fu and Liou*, 1993]. We have modified the δ4S RTM to include sea salt optical properties [*d'Almeida et al.*, 1991] (see section 3.1.3) and dust optical properties derived from PRIDE [*Christopher et al.*, 2003]. Our recent studies indicate an excellent agreement between calculated and observed downward shortwave irradiance at the surface, with differences of <3% when aerosol effects are carefully considered in the δ4S RTM calculations [*Christopher et al.*, 2003].

3.1.2. Aerosol Transport

[14] The RAMS provides a generalized framework for advection and diffusion of three-dimensional scalar quantities. In addition to scalar fields such as temperature and water vapor as routinely used in standard computations, the RAMS allows for specification of up to a hundred additional scalars. The aerosol processes, including emission, advection, and deposition, can be expressed as

$$\frac{\partial C}{\partial t} = -u\frac{\partial C}{\partial x} - v\frac{\partial C}{\partial y} - w\frac{\partial C}{\partial \sigma} - \frac{\partial}{\partial x}\left(K_H\frac{\partial C}{\partial x}\right) - \frac{\partial}{\partial y}\left(K_H\frac{\partial C}{\partial y}\right) - \frac{\partial}{\partial \sigma}\left(K_L\frac{\partial C}{\partial \sigma}\right) + S, \quad (1)$$

where C is the aerosol concentration; u, v, and w are the 3-D wind components; x, y, and σ denote 3-D coordinates; S denotes net source/sink; K_L and K_H are the vertical and horizontal diffusion exchange coefficient, and t is time. While the advection module including diffusion exchange of scalar variables is already available in the RAMS, new emission/deposition parameterizations are incorporated into the model for aerosol transport.

[15] Sea salt and dust aerosols are two primary types of aerosols in the atmosphere during PRIDE [*Reid et al.*,

2003]. In this study, the sea salt concentrations are diagnosed as a function of wind speeds near the ocean surface by using the following formula [*Blanchard and Woodcock*, 1980; *Collins et al.*, 2001]:

$$C(z) = 5\left(6.3 \times 10^{-6} z\right)^{(0.21-0.29\log_{10} U_{10})}, \tag{2}$$

where $C(z)$ is the sea salt concentration (in units of μg m^{-3}) at height z (in meters) above sea level and U_{10} is the 10 m wind speed (m s^{-1}). Above 300 m the profile decreases exponentially with a 500 m scale height.

[16] During the long-range transport of Saharan dust to the Puerto Rico regions, large particles (diameter >10 μm) are deposited either in the source regions or in the ocean near the West African coast. *Schütz and Jaenicke* [1974] found that nearly 75% of the large dust particles are deposited in the source area, leaving only 25% to reach the ocean 1500 km away. During PRIDE, *Maring et al.* [2003] found that dust particles larger than 7.3 μm are mostly removed during the transport. Further analysis showed that the vertical variations of the normalized dust size distribution are usually small during the dust events in PRIDE [*Reid et al.*, 2003], implying that it is reasonable to simulate the mass concentration of dust aerosols in the model rather than simulate the size distribution and use the effective radius as the measure to calculate the gravitational settling. This is especially useful for a case study in temporal scales of 2–3 days. The current model considers the dry deposition process outlined by *Slinn and Slinn* [1980]. Wet deposition process is not included in the simulation because no precipitation was recorded during the period of study. The spatial distribution of GOES 8 AOT is used to initialize the 3-D aerosol concentration fields in the RAMS. The procedure for deriving the 3-D aerosol concentrations from GOES 8 AOTs is described in detail in section 3.2.

3.1.3. Aerosol Optical Property Model

[17] The aerosol optical property model is used to convert aerosol mass concentration into column AOT, thus providing a method for comparison between satellite and simulated AOT. In addition, the spatial distribution of AOT in each model layer is required in radiative transfer calculations. The relationship between mass concentration and AOT can be expressed as

$$\tau = \sum_{i=1}^{K}\left(\tau_{i,\mathrm{dust}} + \tau_{i,\mathrm{salt}}\right) = \sum_{i=1}^{K}\left(Q_{\mathrm{ext,dust}} C_{i,\mathrm{dust}} + Q_{\mathrm{ext,salt}} C_{i,\mathrm{salt}}\right)\Delta z_i, \tag{3}$$

where i is the index for vertical layers, K is the total number of layers in the model, C is the mass concentration of aerosols (g m^{-3}), Q_{ext} is the mass extinction coefficient (m^2 g^{-1}), and Δz_i is the thickness (m) between different layers. In this study, wavelength-dependent dust radiative properties (e.g., single scattering albedo, asymmetric factor, extinction cross section, and mass extinction efficiency) in the shortwave spectrum (0$\sim$4 μm) derived from PRIDE [*Wang et al.*, 2003; *Christopher et al.*, 2003] and in the longwave spectrum from *d'Almeida et al.* [1991] are used. For sea salt aerosols the complex refractive indices from A. A. Lacis (Database of Aerosol Spectral Refractive Indices, Global Aerosol Climatology Project, data available at http://gacp.giss.nasa.gov/data_sets/), the sea salt size distribution during PRIDE from *Maring et al.* [2003], and the geometric growth factor at different relative humidity due to the hygroscopic effect from *d'Almeida et al.* [1991] are utilized in Mie calculations to compute the sea salt radiative properties.

3.2. Assimilation of GOES 8 AOT

[18] The model initialization of aerosol field at regional scales is a challenging process, especially when the study area is not in the aerosol source region. There are two ways to tackle this problem. In the first method the aerosol concentration from large-scale models can be used as initial conditions for the mesoscale model [*Colarco et al.*, 2003]. However, compared to normal meteorological observations, the current in situ aerosol observations are limited. Therefore large uncertainties in dust concentrations could be introduced when using output from global aerosol models as initial conditions for mesoscale aerosol models for short-term aerosol simulations. The second method is to use aerosol information from satellite retrievals as the initial condition [*Westphal and Toon*, 1991]. The advantage of this second method is that the satellite data better represent the aerosol spatial distributions, especially over large areas in cloud-free conditions. The disadvantage is that current satellite aerosol retrievals do not contain vertical information and therefore it is difficult to infer the 3-D aerosol field from 2-D satellite retrievals. As a consequence the shape of aerosol vertical profiles together with a model of aerosol optical properties (section 3.1.3) is required to convert the 2-D AOT into the 3-D aerosol mass concentrations. This study uses the shape of the aerosol concentration profile as measured by aircraft instruments [*Reid et al.*, 2003]. The initial dust profile in each model grid column has the same shape as that derived from aircraft data but has different mass concentrations such that when converting them into AOT using equation (3), the AOT matches the GOES 8 AOT at that grid point. Note, in equation (3), sea salt concentration is diagnosed from wind fields, and the only unknown variable is dust concentration. With known vertical profile shape and GOES 8 AOT on the left side of equation (3) the dust concentration profile for each grid column can be computed.

[19] The justification for the above initialization method is as follows. First of all, it is desirable to have the shape of aerosol vertical profile in the conversions from 2-D AOT field to the 3-D aerosol mass concentration field. The data from aircraft measurements represent the most accurate description of the aerosol vertical profile, especially for the current study where the study area is relatively small and dust vertical profile could have small spatial variations after its long-distance transport across the Atlantic. Therefore the aerosol profile from aircraft measurements is valuable and cannot be ignored in the model initialization. Second, our purpose in this study is to see how the direct consideration of aerosol radiative effects in the model will affect the simulation. In this context, column AOT is more important than the vertical distribution itself. Studies have shown that for aerosols in the lower boundary (<3 km) the vertical distribution of aerosols has little effect on the calculation of

shortwave radiative energy at the surface as long as the column AOT is the same [*Liao and Seinfeld*, 1998]. Therefore using aircraft vertical profile for the initialization purposes is appropriate for this particular case.

[20] After the initialization the mass concentration of aerosols is simulated, and AOT is predicted in each model time step. To assimilate the GOES 8 AOT into the model this study uses a Newtonian nudging scheme where the values of model-predicted AOT tendency are adjusted and the simulated AOTs are relaxed toward the satellite-retrieved AOT:

$$\left[\frac{\partial \tau'_{\mathrm{mod-dust}}}{\partial t}\right]_t = (1-\varepsilon)\left[\frac{\partial \tau_{\mathrm{mod-dust}}}{\partial t}\right]_t + \varepsilon\frac{[\tau_{\mathrm{GOES}}]_{t+1} - [\tau_{\mathrm{mod\text{-}salt}} + \tau_{\mathrm{mod\text{-}dust}}]_t}{\delta\Delta t}. \quad (4)$$

[21] In equation (4), $\partial\tau'_{\text{mod-dust}}/\partial t$ is the updated tendency of simulated dust AOT for the time step t after the assimilation, $\tau_{\text{mod-dust}}/\partial t$ is the tendency of dust AOT at time step t before the assimilation, and $\tau_{\text{mod-salt}}$ is the optical thickness of sea salt. The GOES 8 AOT at time step t + 1 (e.g., $[\tau_{\text{GOES}}]_{t+1}$) is computed by linear interpolation of GOES 8 AOT from the two assimilation time periods (see section 4). The difference between $[\tau_{\text{GOES}}]_{t+1}$ and the simulated AOT (sum of $\tau_{\text{mod-salt}}$ and $\tau_{\text{mod-dust}}$) at time step t divided by the integration time interval Δt is the AOT time tendency if we want to force the modeled AOT to match the GOES 8 AOT in the next step t + 1 (recall $\tau_{t+1} = \tau_t$ + tendency $\times$ Δt). This tendency is then adjusted by a confidence factor (δ), where smaller δ (nearly equal to 1) implies that GOES 8 AOT has very high accuracy, hence larger confidence of this tendency term. The ε value in equation (4) is a 2-D weighting factor that is used in the RAMS to control the effect of the nudging term as a function of spatial location. Notice, for δ = 1 and ε = 1 the effect of the modeled AOT tendency $\partial\tau_{\text{mod-dust}}/\partial$t will be neglected, and equation (4) forces the modeled AOT to exactly relax toward the GOES 8 AOT. We set δ = 1.02 because GOES 8 AOT has a slight overestimate bias when compared to ground and in situ measurements [*Wang et al.*, 2003]. Since this study does not have aerosol fields outside the GOES 8 AOT coverage domain, it is desirable for the nudging term to have maximum effect along the lateral boundaries (to provide the aerosol source) while letting the effect of nudging be minimized in the model interior, allowing for the aerosol transport parameterization. Such behavior is obtained by specifying ε to be nearly one for the five nearest grid points to the lateral boundaries while exponentially decreasing it to zero at grid points in the model interior.

[22] Through the assimilation of GOES 8 AOT the modeled AOT tendency is then optimally modified using equation (4), and consequently, the modeled dust concentration tendency in each layer needs to be adjusted in order to be consistent with the updated AOT tendency. Since the AOT is a column quantity, assumptions on the aerosol vertical distribution must be made in order to adjust the tendency of mass concentration in each layer. In the assimilation of advanced very high resolution radiometer (AVHRR) AOT in CTMs, *Collins et al.* [2001] assumed that the shape of aerosol vertical distribution is the same before and after the assimilation, and thus a scale factor η can be obtained for each model layer i:

$$\eta = \left[\frac{\tau'_{\text{mod-dust}}}{\tau_{\text{mod-dust}}}\right]_{t+1} = \left[\frac{C'_{i,\text{dust}}}{C_{i,\text{dust}}}\right]_{t+1}, \quad (5)$$

where $C'_{i,\text{dust}}$ and $C_{i,\text{dust}}$ are the mass concentration of dust after the assimilation and before the assimilation at layer i, respectively. Therefore from equation (5) the new dust concentration tendency after the assimilation can be calculated using

$$\begin{gathered}[C_{i,\text{dust}}]_t + \left[\frac{\partial C'_{i,\text{dust}}}{\partial t}\right]_t \Delta t = \eta\left[\left(C_{i,\text{dust}}\right)_t + \left(\frac{\partial C_{i,\text{dust}}}{\partial t}\right)_t \Delta t\right] \\ \left[\frac{\partial C'_{i,\text{dust}}}{\partial t}\right]_t = \eta\left[\frac{\partial C_{i,\text{dust}}}{\partial t}\right]_t + \frac{\eta - 1}{\Delta t}[C_{i,\text{dust}}]_t. \end{gathered} \quad (6)$$

[23] In summary, aerosol initial fields are obtained by converting the 2-D GOES 8 AOT into 3-D fields with the assumption that the vertical profiles are the same as prescribed by aircraft measurements in all grids. In the following simulations the dust concentration field is adjusted so that the modeled AOT is relaxed toward the GOES 8 AOT. Therefore except in the initial time step the vertical profiles of aerosol concentration change with time in the different grids.

4. Model Configuration and Initialization

[24] The numerical simulation in this study utilizes a nested grid configuration: a fine grid of 34 $\times$ 34 points and 40 km grid spacing covering the island of Puerto Rico, nested within a coarse grid with 32 $\times$ 32 grid points and 80 km grid spacing (Figure 1). Both the configurations use a stretched vertical grid of 30 grid points and a grid stretch ratio of 1.2, with the vertical grid spacing increasing from 100 m near the surface to a maximum of 750 m higher up in the atmosphere. All numerical simulations used in this study are initiated at 1200 UTC on 20 July 2000 and end at 1200 UTC on 23 July 2000. Time steps of 60 and 10 s are used for time stepping the coarse and fine grids, respectively. Analysis of meteorological fields derived from NCEP reanalysis gridded pressure level data [*Kalnay et al.*, 1996] as well as upper atmospheric and surface observations at 1200 UTC on 20 July 2000 is used to initialize atmospheric conditions in the model simulation. Sea surface temperature is initialized using the AVHRR sea surface temperature (SST) product (J. Vazquez et al., NOAA/NASA advanced very high resolution radiometer (AVHRR) Oceans Pathfinder Sea Surface Temperature Data Set User's Reference Manual Version 4.0, JPL Publication D-14070, available at http://www.nodc.noaa.gov/woce_V2/disk13/avhrr/docs/usr_gde4_0_toc.htm) available at a temporal frequency of 7 days. The SST is assumed to vary linearly with time for the period in between the observations. Similar meteorological analyses at 6 hour intervals are used to nudge the model's lateral and top boundaries. The GOES 8 AOT is produced at 4 $\times$ 4 km [*Wang et al.*, 2003]. Three-dimensional aerosol concentration fields derived

from GOES 8 data valid at 1200 UTC are then averaged into 40 and 80 km grids to initialize aerosol fields in the model. Although GOES 8 AOT has a temporal resolution of a half hour, the model only assimilates the GOES 8 AOT twice per day, one at 1331 UTC and one at 1931 UTC (on the first day, only 1931 UTC is assimilated). There are several reasons for this implementation. First, the GOES 8 AOT at certain time periods are needed for intercomparison with model simulations; otherwise it is difficult to judge the performance of a model only on the basis of the comparison with ground-based point measurements [*Chin et al.*, 2002]. Second, if the model assimilates AOT every half hour, the model simulation will lack its value and will be forced too much toward the GOES 8 AOT. Finally, our near-future goal is to assimilate the MODIS AOT from both Terra and Aqua [*Kaufman et al.*, 2002] into the model, and assimilation of GOES 8 AOT twice per day provides a prototype for our future studies.

[25] Two different numerical simulations are considered in this study, and they differ only in the treatment of aerosol radiative effects, i.e., inclusion of aerosol effects (aero-rad case) and no inclusion of aerosol effects (noaero-rad case). In addition, a ‘‘free-run’’ simulation without any assimilation of GOES 8 AOT but with direct online consideration of aerosol radiative effects is also performed to test the impact of assimilation.

5. Results

[26] The AOT from the numerical simulations is compared against the satellite-derived AOT and point measurements of AOT derived from ground-based Sun photometer. Surface measurements of downward shortwave and longwave fluxes and 2 m air temperature are compared against the simulated values. The differences of AOT and surface radiative energy budget between aero-rad and noaero-rad cases are further compared and analyzed over the whole simulation domain at different time periods.

5.1. Comparison of Modeled AOTs

[27] Satellite observations show that dust approached Puerto Rico during the morning of 20 July 2000 (Figure 2, A1) and reached the island of Puerto Rico in the evening (Figure 2, A2). The dust layer then passed through the island between late evening on 20 July 2000 (Figure 2, A3) to late evening on the second day (Figure 2, A4) and ended by 22 July 2000 (Figure 2, A5). The modeled AOT without any assimilation are shown in Figure 2, B1–B5. In the absence of nudging along the lateral boundaries, the model does not account for external transport of dust into the computational domain. In this case, as shown in Figure 2, B1–B5, the dust layer moves quickly across the model domain and disappears completely in one day. This is a typical behavior for a limited area model without proper specification of boundary conditions.

[28] With assimilation the two numerical model simulations (aero-rad and noaero-rad cases) exhibit spatial patterns of AOT similar to GOES 8 observations (only aero-rad case is shown in Figure 2, C1–C5). Simulated AOT fields from the second grid of the aero-rad case show a very similar sequence of events (Figure 2, C1–C5), and the location of dust front in the model simulation agrees well with that from

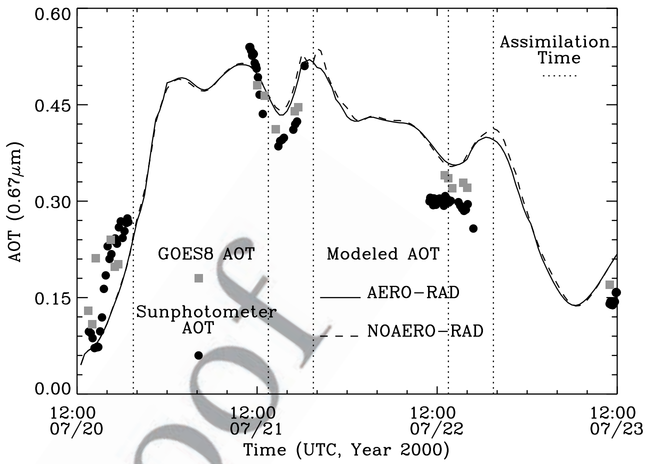

Figure 3. Simulated AOT versus Sun photometer AOT (dots) at La Paguera. Also shown is the GOES 8 AOTs (squares). Vertical dotted line shows the times (1331 and 1991 UTC on each day) when GOES AOT is assimilated into the model.

satellite-retrieved AOT. Note that the satellite-retrieved AOT is plotted at a spatial resolution of 4 km, while the simulated AOT field has a grid spacing of 40 km. Because of these differences the simulated AOT field is smoother compared to observations and lacks some of the observed smaller-scale details (e.g., Figure 2, A3).

[29] Comparison of point observations of AOT derived from Sun photometer measurement at LP against AOT from the closest grid point in model simulations (Figure 3) shows general agreement. The modeled AOT matches the Sun photometer AOT and captures the temporal evolution of dust event very well. Note that the model simulated values are an average over a 40 $\times$ 40 km area while the observations are essentially point measurement that resolves fine-scale features within the dust event. Also notice that the GOES 8 AOT used in this study slightly overestimates the Sun photometer AOT that can result in a positive bias in modeled AOT (Figure 3). During the simulations a total of seven GOES 8 AOT retrievals are assimilated, at 1331 and 1931 UTC as indicated by dotted vertical lines in Figure 3. Though simple linear nudging technique (see equation (3)) is used in this study, the nudging provides a correction for the dynamical simulations in the models. Thus the final results combine the strengths of both nudging corrections and model simulations and therefore are not a simple linear process. Such nonlinear features are distinct, as the modeled AOT can capture the diurnal variations of AOT very well (Figure 3), especially when the dust reaches Puerto Rico. We argue that using linear nudging alone will not produce such a feature since the modeled AOT is the composite effect from both dynamical modeling and the correction from satellite measurements. The implication of Figure 3 is that the best estimation of AOT, especially the diurnal change of AOT, should come from combined satellite measurements and numerical simulations.

[30] Figure 3 also shows that the difference of modeled AOT in aero-rad and noaero-rad cases is visually small, though the AOT difference of $\sim$0.03 does exist at some time periods. The aerosol radiative effects on the simulation

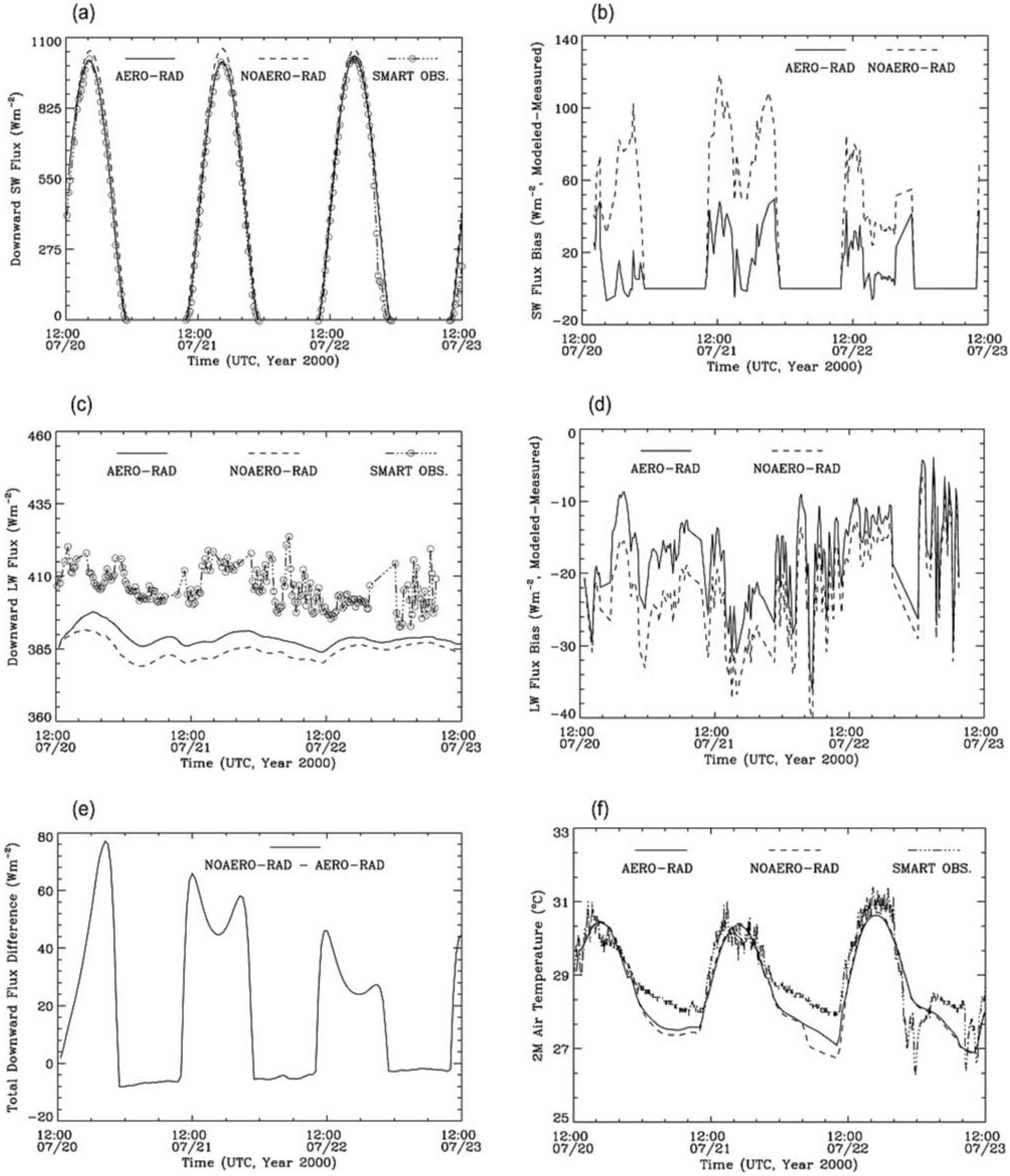

Figure 4. Comparison between measured and modeled downward fluxes at Roosevelt Road in aero-rad and noaero-rad cases for (a) shortwave (SW) and (c) longwave (LW) flux. The differences of modeled and measured downward fluxes are shown for (b) shortwave and (d) longwave fluxes. (e) Total flux difference (e.g., shortwave difference plus longwave difference) between the two simulation cases is shown. All circles denote the in situ data measured from the Surface Measurements for Atmospheric Radiative Transfer (SMART) instrument suite. (f) Comparison between modeled 2 m air temperature with the measured values is shown. See color version of this figure at back of this issue.

of AOTs are then further investigated in terms of the relative difference (in percentage) of AOT in two simulations (e.g., $(\tau_{\text{noaero-rad}} - \tau_{\text{aero-rad}})/\tau_{\text{aero-rad}} \times 100\%$, Figure 2, D1–D5) in the whole model domain. Overall, the relative difference is within $-5\sim10\%$, and the lack of consideration of aerosol radiative effect during the simulation tends to produce a positive bias of AOT. The largest differences occur in areas with low AOTs dominated by sea salt. The maximum absolute difference of AOT is $\sim$0.05 in areas where dust is dominant. As will be shown later, the noaero-rad case overestimates the total downward flux at the surface, and such overestimation causes different atmosphere responses which then leads to differences in modeled AOTs. Even though the atmosphere system responds to aerosol forcing in multiple ways, this study focuses on the impact of dust aerosols on surface radiative energy budget.

5.2. Downward Flux Comparisons

[31] Figure 4a shows the comparison of modeled and measured downward solar flux at the surface at Roosevelt Road, and their difference is shown in Figure 4b. Though both simulations tend to overestimate the downward fluxes, the overestimation in the aero-rad case is much smaller than that in the noaero-rad cases. Note that the measured SW flux only covers a section of the solar spectrum from 0.28$\sim$2.8 μm, while the modeled flux shown in Figure 4b covers the whole SW spectrum (e.g., 0$\sim$4 μm). This partially explains the difference of observed flux and modeled fluxes in the aero-rad case. Using the same dust optical properties and Sun photometer AOTs, off-line calculations indicate that the difference between δ4S RTM modeled SW flux (at 0.28$\sim$2.8 μm) and measured flux is within 15 W m^{-2} [*Christopher et al.*, 2003]. Uncertainties in the modeled AOTs are another factor that potentially contributes to overestimation of downward solar flux by the aero-rad case. Accounting for these two factors and other factors such as the possible presence of cloud (e.g., a sudden sharp drop of measured SW flux in the late afternoon of 22 July), the aero-rad case better represents the averaged downward flux. Compared to the aero-rad simulation and observations, the neglect of scattering by aerosols in noaero-rad case leads to overestimation of instantaneous flux from 10 up to 100 W m^{-2} depending on the magnitude of dust AOTs and time of day (e.g., solar zenith angle, Figure 4b). This is a common feature for most mesoscale models that do not include radiative interactions of aerosols [e.g., *Chen and Dudhia*, 2001]. Overall, the lack of consideration of aerosol radiative effect results in enhancement of solar energy at the surface, with an average daytime "warming" bias of 40 W m^{-2} that is also consistent with the previous studies [*Christopher et al.*, 2003].

[32] Dust absorbs in the longwave part of the electromagnetic spectrum [*d'Almeida et al.*, 1991], and this effect is obvious when comparing the model-simulated downward longwave flux and surface observations (Figures 4c and 4d). The dust layer absorbs the outgoing longwave flux from the surface and reemits it back to the surface, thus increasing the downward longwave flux. Both simulations underestimate the downward longwave fluxes (Figure 4c), but the aero-rad case shows the least deviation from the observations. Note that the simulated downward longwave flux represents an area averaged over 40 $\times$ 40 km while observations are essentially point measurement. The uncertainties in the vertical distribution and dust properties as well as the surface heterogeneity (see section 5.3) could also contribute to the relatively large bias of modeled longwave flux. Compared to the aero-rad simulation, the noaero-rad simulations exhibit a "cool" bias (less downward longwave) at the surface (Figure 4d). The difference is about -10 W m^{-2} depending on the magnitude of AOTs.

[33] The comparison of the total flux difference (shortwave plus longwave) is highly variable depending on the magnitude of AOT and the local time (Figure 4e). Figure 2, E1–E5, shows that the total downward flux difference is highly consistent with the transport of dust aerosols. During the daytime the lack of aerosol radiation effect leads to an overestimation of surface incoming energy from 40$\sim$60 W m^{-2}, though the instantaneous values depend on locations and local time. During the nighttime, however, the surface incoming energy is underestimated $\sim$10 W m^{-2} if dust aerosol radiative effects are not considered. Since these energy fluxes are crucial inputs for the land surface parameterization, the performance of radiative transfer parameterizations used in mesoscale models needs to be further evaluated, which is beyond the scope of the current study.

5.3. Comparison of Air Temperatures

[34] The comparison of the modeled and measured 2 m air temperature is shown in Figure 4f. Figure 4f shows a consistent pattern where the model-simulated nocturnal temperatures are lower than measurements. This is consistent with surface radiation energy budget analysis discussed in section 5.2, which shows underestimation of downward longwave flux, a dominant control on the nocturnal evolution of surface air temperature. During daytime, modeled temperature in both cases has a similar magnitude wit the observations. Overall, since downward flux is overestimated in noaero-rad case during daytime and underestimated during nighttime, the temperature in noaero-rad simulations is slightly higher than that of aero-rad cases in daytime and lower at nighttime. However, such differences are very small, and it is difficult to judge which one is better if solely based on Figure 4e. The reason for this small difference is due to the surface heterogeneity associated with the model grid point covering the Roosevelt Road location. Roosevelt Road is located on the eastern edge of Puerto Rico (Figure 1), and the nearest grid point covers a 40 $\times$ 40 km area that includes both land and ocean. Compared to water bodies, the temperature in the boundary layer over land is significantly more sensitive to changes in surface radiative energy budget. Water bodies absorb downward radiative energy over a deep layer, and mixing transports the energy to further depths. In addition, the high heat capacity of water causes a comparatively slow change in water temperature. In the RAMS, SST is not predicted but is specified using the AVHRR ocean surface temperature product (J.Vazquez et al., NOAA/NASA advanced very high resolution radiometer (AVHRR) Oceans Pathfinder Sea Surface Temperature Data Set User's Reference Manual Version 4.0, JPL Publication D-14070, available at http://www.nodc.noaa.gov/woce_V2/disk13/avhrr/docs/usr_gde4_0_toc.htm). The RAMS uses linear interpolation to account for variations in SST over a timescale of a week, but the diurnal variations are not explicitly simulated.

However, note that the diurnal and short-timescale (2∼3 days) variations in SST are expected to be negligible because of reasons discussed above. Over land, the downward radiation is absorbed by a thin layer of surface soil, and small soil heat capacity causes rapid changes in soil temperature compared to a water surface. Convective mixing efficiently transports a major part of the energy absorbed by the land surface to the boundary layer, resulting in it being more responsive to changes in surface radiative energy budgets. Therefore at the grid point used for comparison against measurements from Roosevelt Road, the impact of aerosol radiative forcing on the 2 m air temperature is diminished because of the presence of ocean in that grid cell.

[35] The aerosol radiative forcing effect on the boundary layer temperature and its modulation by the nature of surface type become more obvious when the temperature difference between two cases in the first model layer above the ground is compared. Figure 2, F1–F5, shows that such temperature difference patterns are correlated to corresponding spatial distribution patterns of AOT. Over ocean, where changes in surface radiation energy budget have negligible effect on boundary layer air temperature, direct heating of air by the absorption of dust aerosols is the dominant process. Therefore presence of atmospheric dust over ocean leads to direct warming of air, causing air temperatures to be warmer in aero-rad case over such region [*Carlson and Benjamin*, 1980]. However, over land, heat transfer from the surface to the atmosphere (either through the sensible heating or the vertical turbulence convection) has the more dominant effect and overshadows the direct radiative heating effect of the atmospheric dust. Decrease in downward solar radiation and associated reduction in sensible heat transfer to the atmosphere over land in the presence of atmospheric dust leads to air temperature being lower in aero-rad case. The neglect of aerosol radiative effect leads to the temperature change in the first model layer from $-0.5°C$ over the ocean to $0.5°C$ over the land when dust is dominant.

6. Discussion and Conclusion

[36] In this study, a method for assimilating the satellite derived AOT into the regional mesoscale models is developed. A four stream radiative transfer parameterization was added into the RAMS to explicitly consider the aerosol radiative effects during the simulation. Through the comparison with in situ, ground-based and satellite observations it is found that the inclusion of aerosol radiative effects improves the overall performance of the modeled aerosol fields and surface radiation budgets, though improvement of 2 m air temperature is minimal because of the relatively coarse grid size that cannot resolve the detailed surface characteristics near the observation site.

[37] The implication of this study is twofold. First, for moderate to high aerosol loadings, aerosol radiative effects and atmospheric response to these effects are significant enough to be considered in the simulation of aerosol transport and weather forecast. Off-line simulations without proper treatment of aerosol radiative feedbacks may exhibit biases which could be severe depending on the aerosol type and loading as well as surface type, consistent with a recent theoretical study which shows that aerosol absorption in the atmosphere could alter the surface radiation energy budget and the profile of heating rate significantly enough to influence the vertical diffusions in the boundary layer [*Yu et al.*, 2002]. Second, since there are only a few observations available that routinely measure the aerosol concentration over the globe, assimilation of satellite aerosol retrievals into the mesoscale numerical models provides an important tool to narrow the uncertainties in aerosol source function and has the potential to become a cost-effective method to improve particulate matter forecast, especially in places where ground-based observations are sparse. One of the major obstacles in this type of assimilation is the lack of information on the vertical structures of aerosol distributions in current satellite aerosol retrievals. Aerosol vertical profiles from spaceborne lidar measurements [*Winker et al.*, 2002] could provide valuable information for the assimilation of satellite-derived AOTs in the near future. Therefore with direct consideration of aerosol radiation effects and assimilation of satellite aerosol retrievals the aerosol transport and distribution can be more realistically simulated, which also has the potential to bring overall improvement to weather forecast.

[38] **Acknowledgments.** This research was supported by NASA's radiation sciences, interdisciplinary sciences, ACMAP, NASA grant NAG5-11941, and National Science Foundation grant ATM-0128924. J. Wang was also supported by the NASA Earth Sciences System Graduate Fellowship Program (ESSF/04-0000-0272). We are grateful to Jeffrey Reid, Hal Maring, Si-Chee Tsay, and Qiang Ji for their PRIDE data sets. We also thank Deepak Ray for his help in the early stages of the model configuration and Qiang Fu, K. N. Liou, and Fred Rose for the δ four stream radiative transfer model.

References

Binkowski, F. S., and S. J. Roselle (2003), Models-3 Community Multiscale Air Quality (CMAQ) model aerosol component: 1. Model description, *J. Geophys. Res.*, *108*(D6), 4183, doi:10.1029/2001JD001409.
Blanchard, D. C., and A. H. Woodcock (1980), Production, concentration, and vertical distribution of the sea salt aerosols, *Ann. N. Y. Acad. Sci.*, *338*, 330–347.
Byun, D. W., and J. K. S. Ching (1999), Science algorithms of the EPA Models-3 Community Multiscale Air Quality (CMAQ) modeling system, *Rep. EPA-600/R-99/030*, U.S. Environ. Prot. Agency, U.S. Govt. Print. Off., Washington, D. C.
Carlson, T. N., and S. G. Benjamin (1980), Radiative heating rate of Saharan dust, *J. Atmos. Sci.*, *37*, 193–213.
Chen, F., and J. Dudhia (2001), Coupling an advanced land surface-hydrology model with the Penn State-NCAR MM5 modeling system. Part I: Model implementation and sensitivity, *Mon. Weather Rev.*, *129*, 569–585.
Chin, M., P. Ginoux, S. Kinne, O. Torres, B. N. Holben, B. N. Duncan, R. V. Martin, J. A. Logan, A. Higurashi, and T. Nakajima (2002), Tropospheric aerosol optical thickness from the GOCART model and comparisons with satellite and Sun photometer measurements, *J. Atmos. Sci.*, *59*, 461–483.
Christopher, S. A., and J. Zhang (2002), Shortwave Aerosol Radiative Forcing from MODIS and CERES observations over the oceans, *Geophys. Res. Lett.*, *29*(18), 1859, doi:10.1029/2002GL014803.
Christopher, S. A., X. Li, R. M. Welch, P. V. Hobbs, J. S. Reid, and T. F. Eck (2000), Estimation of downward and top-of-atmosphere shortwave irradiances in biomass burning regions during SCAR-B, *J. Appl. Meteorol.*, *39*, 1742–1753.
Christopher, S. A., J. Zhang, B. N. Holben, and S.-K. Yang (2002), GOES 8 and NOAA-14 AVHRR retrieval of smoke aerosol optical thickness during SCAR-B, *Int. J. Remote Sens.*, *23*, 4931–4944.
Christopher, S. A., J. Wang, Q. Ji, and S. Tsay (2003), Estimation of diurnal shortwave dust aerosol radiative forcing during PRIDE, *J. Geophys. Res.*, *108*(D19), 8596, doi:10.1029/2002JD002787.
Colarco, P. R., O. B. Toon, and B. N. Holben (2003), Saharan dust transport to the Caribbean during PRIDE: 1. Influence of dust sources and removal mechanisms on the timing and magnitude of downwind aerosol optical

depth events from simulations of in situ and remote sensing observations, *J. Geophys. Res.*, *108*(D19), 8589, doi:10.1029/2002JD002658.
Collins, W. D., P. J. Rasch, B. E. Eaton, B. V. Khattatov, and C. S. Zender (2001), Simulating aerosols using a chemical transport model with assimilation of satellite aerosol retrievals: Methodology for INDOEX, *J. Geophys. Res.*, *106*, 7313–7336.
Cotton, W. R., et al. (2002), RAMS 2001: Current status and future directions, *Meteorol. Atmos. Phys.*, *82*, 5–29, doi:10.1007/s00703-001-0584-9.
d'Almeida, G. A., P. Koepke, and E. P. Shettle (1991), *Atmospheric Aerosols: Global Climatology and Radiative Characteristics*, p. 561, A. Deepak, Hampton, Va.
Duce, R. (1991), The atmospheric input of trace species to the world ocean, *Global Biogeochem. Cycles*, *5*, 193–259.
Fu, Q., and K. N. Liou (1993), Parameterization of the radiative properties of cirrus clouds, *J. Atmos. Sci.*, *50*, 2008–2025.
Ginoux, P., M. Chin, I. Tegen, J. M. Prospero, B. Holben, O. Dubovik, and S.-J. Lin (2001), Sources and distributions of dust aerosols simulated with the GOCART model, *J. Geophys. Res.*, *106*, 20,255–20,273.
Hansen, J. E., and A. A. Lacis (1990), Sun and dust versus greenhouse gases: An assessment of their relative roles in global climate change, *Nature*, *346*, 713–719.
Ji, Q., and S.-C. Tsay (2000), On the dome effect of Eppley pyrgeometers and pyranometers, *Geophys. Res. Lett.*, *27*, 971–974.
Kalnay, E., et al. (1996), The NCEP/NCAR 40-year reanalysis project, *Bull. Am. Meteorol. Soc.*, *77*, 437–471.
Kaufman, Y. J., D. Tanre, and O. Boucher (2002), A satellite view of aerosols in climate systems, *Nature*, *419*, 215–223.
Liao, H., and J. H. Seinfeld (1998), Radiative forcing by mineral dust aerosols: Sensitivity to key variables, *J. Geophys. Res.*, *103*, 31,637–31,645.
Liou, K. N., Q. Fu, and T. P. Ackerman (1988), A simple formulation of the δ-four-stream approximation for radiative transfer parameterizations, *J. Atmos. Sci.*, *45*, 1940–1947.
Maring, H., D. L. Savoie, M. A. Izaguirre, L. Custals, and J. S. Reid (2003), Mineral dust aerosol size distribution change during atmospheric transport, *J. Geophys. Res.*, *108*(D19), 8592, doi:10.1029/2002JD002536.
Pielke, R. A., R. L. Walko, J. L. Eastman, W. A. Lyons, R. A. Stocker, M. Uliasz, and C. J. Tremback (1992), A comprehensive meteorological modeling system - RAMS, *Meteorol. Atmos. Phys.*, *49*, 69–91.
Prospero, J. M. (1999), Long-term measurements of the transport of African mineral dust to the southeastern United States: Implications for regional air quality, *J. Geophys. Res.*, *104*, 15,917–15,927.
Reid, J. S., et al. (2003), Analysis of measurements of Saharan dust by airborne and ground-based remote sensing methods during the Puerto Rico Dust Experiment (PRIDE), *J. Geophys. Res.*, *108*(D19), 8586, doi:10.1029/2002JD002493.
Schütz, L., and R. Jaenicke (1974), Particle number and mass distribution above 10–4 cm radius in sand and aerosol of the Sahara desert, *J. Appl. Meteorol.*, *13*, 863–870.
Shinn, E. A., G. W. Smith, J. M. Prospero, P. Betzer, M. L. Hayes, V. Garrison, and R. T. Barber (2000), African dust and the demise of Caribbean coral reefs, *Geophys. Res. Lett.*, *19*, 3029–3032.
Slinn, S. A., and W. G. N. Slinn (1980), Predictions for particle deposition on natural waters, *Atmos. Environ.*, *14*, 1013–1016.
Takemura, T., H. Okamoto, Y. Maruyama, A. Numaguti, A. Higurashi, and T. Nakajima (2000), Global three-dimensional simulation of aerosol optical thickness distribution of various origins, *J. Geophys. Res.*, *105*, 17,853–17,873.
Tegen, I., and I. Fung (1994), Modeling of mineral dust in the atmosphere: Sources, transport, and optical thickness, *J. Geophys. Res.*, *99*, 22,897–22,914.
Walko, R. L., et al. (2000), Coupled atmosphere-biophysics-hydrology models for environmental modeling, *J. Appl. Meteorol.*, *39*, 931–944.
Wang, J., and S. A. Christopher (2003), Intercomparison between satellite-derived aerosol optical thickness and $PM_{2.5}$ mass: Implications for air quality studies, *Geophys. Res. Lett.*, *30*(21), 2095, doi:10.1029/2003GL018174.
Wang, J., S. A. Christopher, J. S. Reid, H. Maring, D. Savoie, B. N. Holben, J. M. Livingston, P. B. Russell, and S. Yang (2003), GOES 8 retrieval of dust aerosol optical thickness over the Atlantic Ocean during PRIDE, *J. Geophys. Res.*, *108*(D19), 8595, doi:10.1029/2002JD002494.
Weaver, C. J., P. Ginoux, N. C. Hsu, M.-D. Chou, and J. Joiner (2002), Radiative forcing of Saharan dust: GOCART model simulations compared with ERBE data, *J. Atmos. Sci.*, *59*, 736–747.
Westphal, D. L., and O. B. Toon (1991), Simulation of microphysical, radiative, and dynamical processes in a continental-scale forest smoke plume, *J. Geophys. Res.*, *96*, 22,379–22,400.
Westphal, D. L., O. B. Toon, and T. N. Carlson (1987), A two-dimensional numerical investigation of the dynamics and microphysics of Saharan dust storms, *J. Geophys. Res.*, *92*, 3027–3049.
Westphal, D. L., O. B. Toon, and T. N. Carlson (1988), A case study of mobilization and transport of Saharan dust, *J. Atmos. Sci.*, *45*, 2145–2174.
Winker, D. M., J. Pelon, and M. P. McCormick (2002), The CALIPSO mission: Spaceborne lidar for observation of aerosols and clouds, *Proc. SPIE Int. Soc. Opt. Eng.*, *4893*, 1–11.
Yu, H., S. C. Liu, and R. E. Dickinson (2002), Radiative effects of aerosols on the evolution of the atmospheric boundary layer, *J. Geophys. Res.*, *107*(D12), 4142, doi:10.1029/2001JD000754.
Yu, H., R. E. Dickinson, M. Chin, Y. J. Kaufman, B. N. Holben, I. V. Geogdzhayev, and M. I. Mishchenko (2003), Annual cycle of global distributions of aerosol optical depth from integration of MODIS retrievals and GOCART model simulations, *J. Geophys. Res.*, *108*(D3), 4128, doi:10.1029/2002JD002717.

S. A. Christopher, U. S. Nair, and J. Wang, University of Alabama in Huntsville, Department of Atmospheric Sciences, 320 Sparkman Drive, Huntsville, AL 35805-1912, USA. (sundar@nsstc.uah.edu)

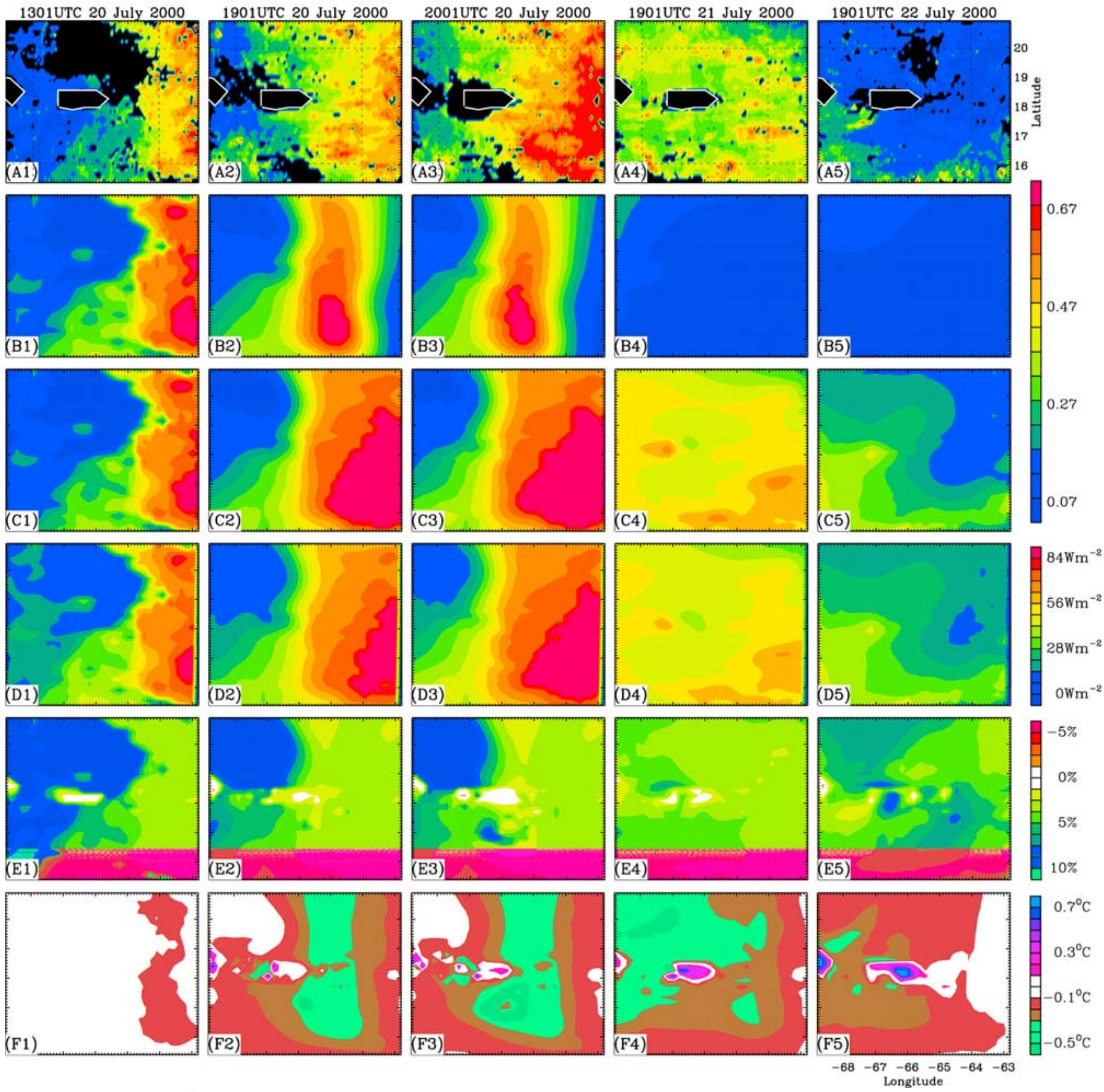

Figure 2. Dust AOT retrieved from GOES 8 (A1–A5) and simulated AOT from the RAMS with (B1–B5) and without (C1–C5) assimilation of GOES 8 AOTs using nudging scheme. The percentage difference in AOT between aero-rad and noaero-rad cases is shown in D1–D5. The total downward radiative flux difference (longwave plus shortwave, W m^{-2}) at the surface and temperature difference (°C) in the model first layer above the surface are shown in E1–E5 and F1–F5, respectively. The black regions in A1–A5 are cloudy regions, and the white-outlined black areas are Puerto Rico land regions.

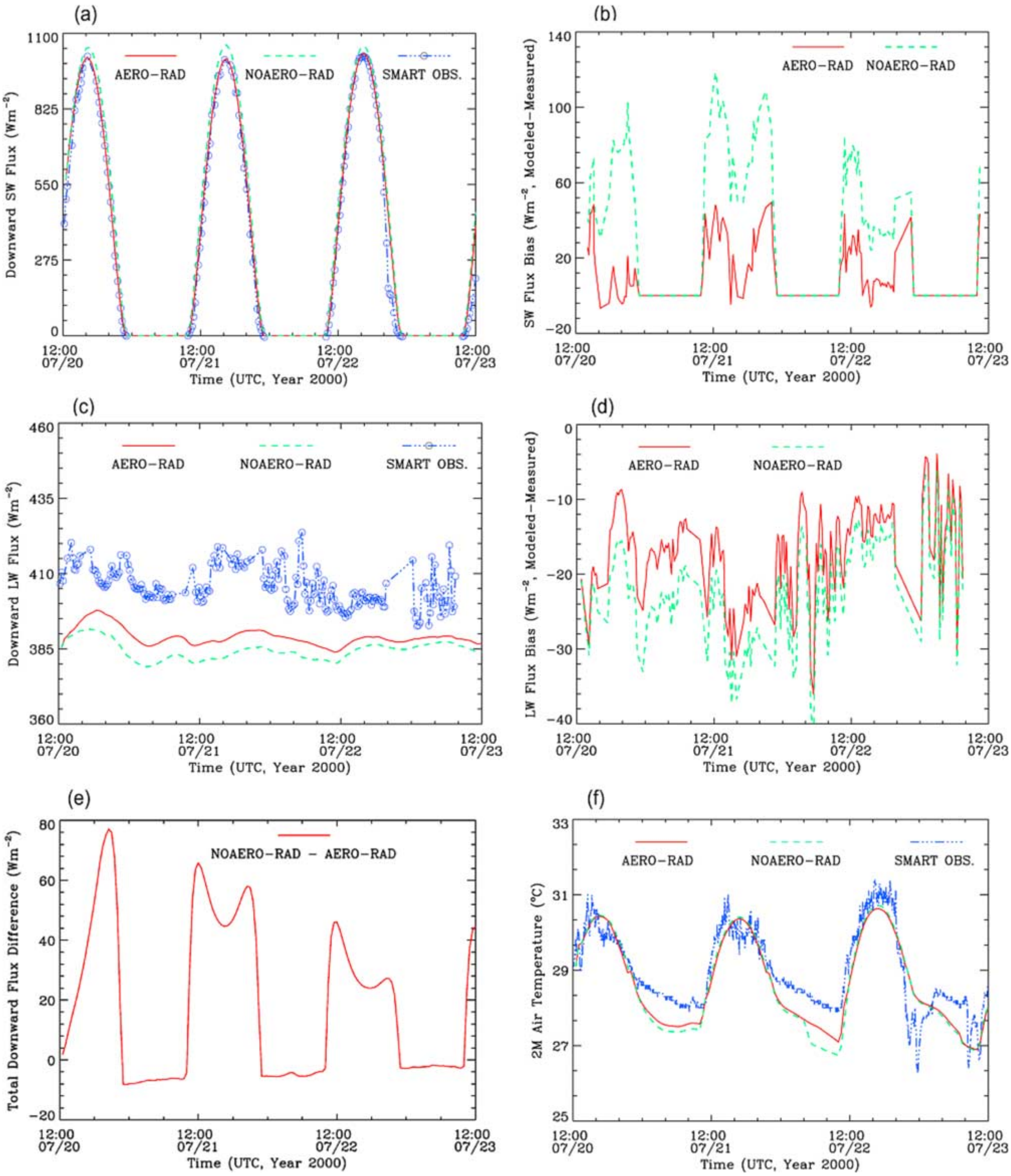

Figure 4. Comparison between measured and modeled downward fluxes at Roosevelt Road in aero-rad and noaero-rad cases for (a) shortwave (SW) and (c) longwave (LW) flux. The differences of modeled and measured downward fluxes are shown for (b) shortwave and (d) longwave fluxes. (e) Total flux difference (e.g., shortwave difference plus longwave difference) between the two simulation cases is shown. All circles denote the in situ data measured from the Surface Measurements for Atmospheric Radiative Transfer (SMART) instrument suite. (f) Comparison between modeled 2 m air temperature with the measured values is shown.